

See discussions, stats, and author profiles for this publication at: <https://www.researchgate.net/publication/263974822>

Crystal Growth of Tl_4CdI_6 : A Wide Band Gap Semiconductor for Hard Radiation Detection

ARTICLE in CRYSTAL GROWTH & DESIGN · MARCH 2014

Impact Factor: 4.89 · DOI: 10.1021/cg5001446

CITATIONS

5

READS

106

11 AUTHORS, INCLUDING:



Zhifu Liu

Northwestern University

73 PUBLICATIONS 680 CITATIONS

SEE PROFILE



John Anthony Peters

University of Dundee

212 PUBLICATIONS 11,655 CITATIONS

SEE PROFILE



Maria Sebastian

Northwestern University

17 PUBLICATIONS 103 CITATIONS

SEE PROFILE



Constantinos C. Stoumpos

Northwestern University

52 PUBLICATIONS 1,490 CITATIONS

SEE PROFILE

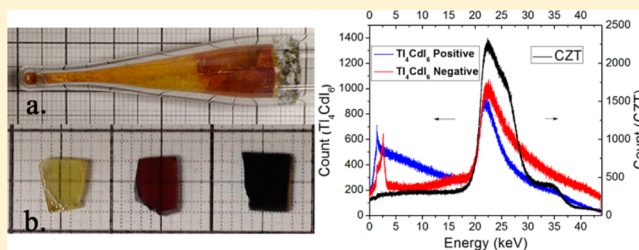
Crystal Growth of Tl_4CdI_6 : A Wide Band Gap Semiconductor for Hard Radiation Detection

Shichao Wang,[†] Zhifu Liu,[‡] John A. Peters,[‡] Maria Sebastian,[†] Sandy L. Nguyen,[†] Christos D. Malliakas,[†] Constantinos C. Stoumpos,[†] Jino Im,[§] Arthur J. Freeman,[§] Bruce W. Wessels,[‡] and Mercouri G. Kanatzidis^{*,†}

[†]Department of Chemistry, [‡]Department of Materials Science and Engineering, and [§]Department of Physics and Astronomy, Northwestern University, Evanston, Illinois 60208, United States

S Supporting Information

ABSTRACT: We report the synthesis, physical characterization, and crystal growth of Tl_4CdI_6 . We show that this material has good photoconductivity and is a promising semiconductor for room temperature X-ray and γ -ray detection. Large single crystals were grown by the vertical Bridgman method and cut to dimensions appropriate for detector testing. Single crystal X-ray diffraction refinements confirm that Tl_4CdI_6 crystallizes in the tetragonal crystal system with a centrosymmetric space group of $P4/mnc$, with a calculated density of 6.87 g/cm^3 . Thermal analysis and high-temperature synchrotron powder diffraction studies were used to determine phase relationships and crystallization behavior during crystal growth. We have elucidated the reason for different colors encountered when synthesizing or growing single crystals of Tl_4CdI_6 (yellow, red, and black), and it is the presence of a small amount of TlI impurity. We report proper crystal growth conditions to obtain essentially pure yellow Tl_4CdI_6 crystals. The material having the yellow color has a band gap of 2.8 eV . First-principles density functional theory calculations indicate a direct band gap at the Γ point of the Brillouin zone. The Tl_4CdI_6 crystals have a resistivity of $10^{10} \Omega\cdot\text{cm}$. Photoconductivity measurements on the as-grown crystals show mobility-lifetime product on the order of $10^{-4} \text{ cm}^2/\text{V}$ for both electrons and holes. The promising detector properties of this material are confirmed by preliminary measurements showing a clear spectral response to an Ag X-ray source, which classifies Tl_4CdI_6 as an emerging material for radiation detection.



INTRODUCTION

Wide band gap semiconductors are attracting attention as hard radiation (X-ray and γ -ray) detectors in high-energy physics, radiochemistry, biomedical imaging, nondestructive testing, γ -ray astronomy, spectroscopic instrumentation, homeland security applications, and other applications.^{1–6} To date, only a few materials have been shown to demonstrate efficient radiation detection at room temperature, including CdTe ,^{7,8} $\text{Cd}_{1-x}\text{Zn}_x\text{Te}$ (CZT),^{9–12} TlBr ,^{13–15} PbI_2 ,^{16,17} and HgI_2 .^{18,19} For room temperature operation, desired radiation detectors require a strict combination of properties in a semiconductor crystal that need to be satisfied simultaneously: high density and high average atomic number (Z) to provide adequate absorption of the incoming radiation, high electrical resistivity and wide band gap ($E_g > 1.6 \text{ eV}$) to minimize dark current and electronic noise, and high crystal quality and high mobility-lifetime ($\mu\tau$) products of the charge carriers for rapid signal readout. Among the above parameters, the $\mu\tau$ product is considered to be a figure of merit for detector materials. Currently, $\text{Cd}_{0.9}\text{Zn}_{0.1}\text{Te}$ is the leading semiconductor material for room temperature detection with a band gap of 1.57 eV , high density, high resistivity, and high $\mu\tau$ products.⁹ However, despite decades of development, growth of large high-quality single crystals of CZT is still a difficult challenge.^{20–26} Some

shortcomings limiting its applications include cracks, Te precipitates, low yields, and low intrinsic hole mobility.^{9,24–26} Efforts on alternative materials are mainly focused on heavy metal halide compounds (PbI_2 , TlBr , HgI_2). These materials have disadvantages such as relatively low $\mu\tau$ products, low hardness, polarization effects, and phase changes.^{27–31} Therefore, new materials are desirable that can detect at room temperature with high signal-to-noise ratios.

From the perspective of materials chemistry, the preferential consideration in designing superior radiation detectors is to identify heavy element semiconductors with wide band gaps. In particular, thallium-containing compounds are promising for radiation detection, because of the high density and high Z that can be attained. This, in turn, increases the absorption coefficient of the materials for X-ray and γ -rays. The concepts of “dimensional reduction” (DR)³² and “lattice hybridization” (LH)³³ recently proposed by our group have proven to be effective materials design tools to predict materials with desired band gaps and density. For example, ongoing intensive studies based on DR and LH have resulted in the discovery of many

Received: January 26, 2014

Revised: March 3, 2014

Published: March 20, 2014



new promising ternary semiconductor compounds that include TlGaSe_2 ,³⁴ Tl_6SeI_4 ,^{33,35} $\text{Cs}_2\text{Cd}_3\text{Te}_4$, $\text{Cs}_2\text{Hg}_3\text{Se}_4$,³² $\text{Cs}_2\text{Hg}_6\text{S}_7$,³⁶ and $\text{Tl}_2\text{Hg}_3\text{Q}_4$ ³⁷ (Q = S, Se, and Te). These compounds exhibit high $\mu\tau$ products and high electrical resistivity, even with modest purification performed on them.

Here, we focused on the known compound Tl_4CdI_6 as a promising candidate for radiation detection. Tl_4CdI_6 , which has been studied previously,^{38–45} melts at 354 °C and crystallizes in the tetragonal $P4/mnc$ structure with the unit cell $a = b = 9.222(4)$ Å and $c = 9.603(4)$ Å.^{42,43} Tl_4CdI_6 has a three-dimensional (3D) structure composed of Tl^+ cations and $[\text{CdI}_6]^{4-}$ anions. The high atomic numbers ($Z_{\text{Tl}} = 81$, $Z_{\text{Cd}} = 48$, and $Z_{\text{I}} = 53$) give this compound a high density of 6.88 g/cm³ and good X-ray and γ -ray stopping power. The attenuation lengths of Tl_4CdI_6 and CZT, as calculated using the atomic attenuation coefficients tabulated by NIST,⁴⁶ indicate that the stopping power and absorption coefficients of Tl_4CdI_6 are significantly greater than that of CZT over most of the photon energy range. The higher attenuation coefficient implies that the requirements on the $\mu\tau$ products can be relaxed and thinner detector dimensions may be expected. Because of these attributes, Tl_4CdI_6 has attracted our attention as a potential detector material.

In this study, we present the synthesis, crystal growth, and physical property characterization of Tl_4CdI_6 . We also analyze the electronic structure of this material using first-principles density functional theory calculations. Large single crystals have been grown by the vertical Bridgman method and cut to dimensions appropriate for detector operation. We find that Tl_4CdI_6 exhibits good detector material properties, including a wide band gap, a high electrical resistivity, and a suitable $\mu\tau$ product for electrons as well as holes, comparable to that of commercial CZT for room temperature applications. Finally, we demonstrate that a detector device made from Tl_4CdI_6 crystals can detect hard X-rays from a Ag X-ray tube source and resolve the Ag K peak energetically.

■ EXPERIMENTAL SECTION

Syntheses. The Tl_4CdI_6 compound was synthesized using TII (99.999% metal basis, Alfa Aesar) and CdI_2 (99.999%, Sigma Aldrich) as starting materials. The reagents TII (3.9174 g, 11.82 mmol) and CdI_2 (1.0826 g, 2.96 mmol) were mixed in stoichiometric ratio in a glovebox under a N_2 protective atmosphere with O_2 and H_2O levels below 0.1 ppm. The mixture was sealed in a fused silica tube ($\Phi 13 \times 180$ mm) under 10^{-4} mbar vacuum and subsequently placed in a temperature-programmable electric furnace. The tube was heated to 450 °C in 12 h and held there for 24 h to ensure a homogeneous melt, followed by rapid cooling (50 °C/h) to 400 °C and slower cooling (10 °C/h) to 250 °C and finally to room temperature after the furnace was turned off. **Caution:** Because of the toxicity of thallium, great care should be exerted with appropriate protective equipment in both the synthesis and handling of the Tl_4CdI_6 crystals. Handling of Tl-containing compounds should be carried out in the glovebox.

Crystal Growth. Bulk Tl_4CdI_6 single crystals were grown by a modified Bridgman–Stockbarger technique employing spontaneous nucleation in a two-zone vertical furnace with an axial temperature gradient of 0.9–1.3 °C/mm. The heating area was divided into two zones by a baffle, and the desired temperature gradient was realized by carefully adjusting the baffle position in the furnace. The ground Tl_4CdI_6 polycrystalline raw material (~10 g) was loaded into a specially designed ($\Phi 13 \times 180$ mm) fused-silica ampule with a conical bottom and sealed under a pressure of 10^{-4} mbar.

Crystal Growth of Tl_4CdI_6 (Yellow). The above-described ampule was first heated to 450 °C in the high temperature zone, and held for 48 h until the polycrystalline Tl_4CdI_6 was fully melted. Then the

growth process was carried out by lowering the ampule at a rate of 1.8 mm/h using a stepping motor. The initial nucleation started from the tip at the bottom when it passed through the hole at the center of the baffle, where the temperature is close to the melting point of Tl_4CdI_6 . The crystal continued to grow with the help of the seed in the tip until the whole ampule was moved into the low temperature zone (250 °C). After the growth, the furnace was slowly cooled to room temperature at a rate of 20 °C/h. No reaction was observed with the fused-silica crucible.

Crystal Growth of Tl_4CdI_6 (Red). The above ampule was first heated to 400 °C in the high-temperature zone and held there for 48 h. Then the growth process was carried out by lowering the ampule at a rate of 0.6 mm/h. The low-temperature zone was set to 250 °C. After the growth, the furnace was slowly cooled to room temperature at a rate of 20 °C/h.

Crystal Growth of Tl_4CdI_6 (Black). The above ampule was first heated to 400 °C in the high-temperature zone and held there for 48 h. Then the growth process was carried out by lowering the ampule at a rate of 0.6 mm/h. The low-temperature zone was set to 150 °C. The ampule was stopped lowering at the position where the temperature was 330 °C, held there for 2 weeks, and then kept on moving. After the growth, the furnace was slowly cooled to room temperature at a rate of 20 °C/h.

The Tl_4CdI_6 ingots were cut into wafers and rectangular blocks using a Struers Accutom-50 waferizing saw equipped with a 300- μm -wide diamond-impregnated blade and subsequently polished with successively finer grit SiC grinding papers, finishing off with a 3 μm particle size sandpaper. The single crystalline nature of the wafers was verified using a polarized light microscope. The single crystals were oriented using Laue X-ray back-reflection that was recorded on an image plate in a home-built setup equipped with white Ag X-ray irradiation. The scanned X-ray diffraction pattern was indexed using the software OrientExpress.⁴⁷

In Situ Temperature-Dependent Synchrotron Powder X-ray Diffraction. Fine powders of a yellow Tl_4CdI_6 compound were sealed in an N_2 -filled Roentgen glass tube. In situ synchrotron XRD ($\lambda = 0.413\,906$ Å) patterns were recorded from room temperature to 356.5 °C at a rate of 20 °C/h using at the 11-BM beamline at the Advanced Photon Source (Argonne, IL).

Detector Properties. Detector properties were analyzed using white radiation from a Ag X-ray tube source (ATPS XRD 1000) with an accelerating voltage of 40 kV and a current of 20 mA. A polished yellow Tl_4CdI_6 wafer with dimensions of 35 mm² surface area and thickness of 1.6 mm was used for detector application. Silver contacts were used for the electrodes of the detector sample. The sample was placed in a model eV-480 test fixture connected to a model eV-550 preamplifier box. The bias voltage was 100 V, corresponding to an electric field of 6.25×10^4 V/m. As a reference detector, one commercial CZT sample with dimensions of $5 \times 5 \times 2$ mm was operated at a bias voltage of 120 V, corresponding to an electric field nearly equal to that applied to the Tl_4CdI_6 sample. The counting time for Tl_4CdI_6 and CZT was 105 s. For both the Tl_4CdI_6 and the CZT detector, the signal was transferred to an ORTEC amplifier (model 572A) with a gain of 500 and shaping time of 0.5 μs before it was evaluated by a dual 16 K input multichannel analyzer (model ASPEC-927). The data was then recorded using MAESTRO-32 software. A schematic of the setup has been reported previously.^{33,34}

■ RESULTS AND DISCUSSION

Synthesis and Crystal Growth. Bulk yellow polycrystalline Tl_4CdI_6 can be synthesized from high-purity starting materials by reacting appropriate stoichiometric ratios of solid TII with CdI_2 at 450 °C. The black impurity phases that appear after reaction on the top part of the melted ingot can be discarded. The remaining Tl_4CdI_6 material is of high purity, as checked by powder X-ray diffraction, and it can be used as raw material for subsequent single crystal growth studies. Using a modified vertical Bridgman growth procedure, several centi-

meter-sized ingots were obtained. An example of a Bridgman-grown ingot of Tl_4CdI_6 is shown in Figure 1a. The single crystal

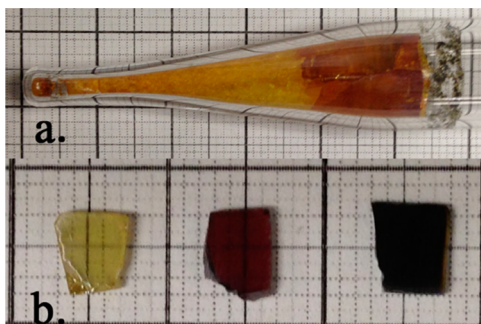


Figure 1. As-grown crystals of Tl_4CdI_6 . (a) Ingot obtained by Bridgman method. (b) Typical single crystals with the colors of yellow, red, and black, which were cut and polished from different ingots.

ingots were observed to grow along the crystallographic c -axis (see Table 1 for crystal data). Consequently, the grown crystals were cut perpendicular and parallel to the growth direction to suitable dimensions and polished. It exhibits robust mechanical properties, because cutting and polishing were readily performed and small stress cracks appeared only rarely. The single crystals are stable in air.

The crystals appear yellow, red, and black (Figure 1b) from different ingots which were grown under different conditions (discussed below). Figure 2 shows the powder XRD patterns

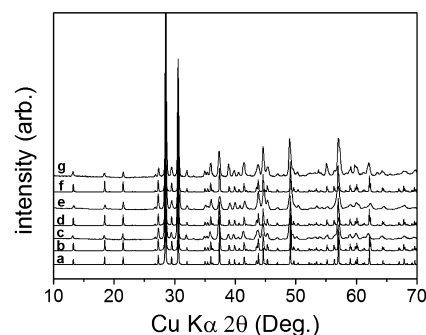


Figure 2. Powder X-ray diffraction (XRD) pattern of Tl_4CdI_6 crystals. (a) Simulation from ICSD. (b) Simulation from yellow single crystal. (c) Yellow ground crystals. (d) Simulation from red single crystal. (e) Red ground crystals. (f) Simulation from black single crystal. (g) Black ground crystals.

for ground crystals of the yellow, red, and black Tl_4CdI_6 specimens. The peak positions match the theoretical diffraction pattern from the reported crystal structure^{42,43} as well as the patterns simulated from the new more accurate single crystal refinement reported here. Thus, we confirmed the essentially single-phase nature of the Bridgman-grown crystals. The EDS compositions are very similar (within experimental error) at “ $\text{Tl}_{3.92}\text{CdI}_{5.88}$ ”, “ $\text{Tl}_{3.75}\text{CdI}_{5.65}$ ”, and “ $\text{Tl}_{3.82}\text{CdI}_{6.12}$ ” for the yellow, red, and black Tl_4CdI_6 samples, respectively. No other impurity elements were found by EDS.

Table 1. Crystal Data and Structure Refinement for Tl_4CdI_6 ^a

	Tl_4CdI_6		
	yellow	red	black
formula mass (amu)	1691.33	1691.33	1691.33
crystal system	tetragonal	tetragonal	tetragonal
space group	$P4/mnc$	$P4/mnc$	$P4/mnc$
a (Å)	9.2309(8)	9.2288(4)	9.2323(6)
b (Å)	9.2309(8)	9.2288(4)	9.2323(6)
c (Å)	9.5945(14)	9.6054(6)	9.6015(11)
V (Å ³)	817.54(19)	818.10(7)	818.39(12)
Z	2	2	2
crystal size (mm)	$0.20 \times 0.20 \times 0.15$	$0.25 \times 0.2 \times 0.12$	$0.15 \times 0.20 \times 0.18$
ρ (calcd)(g/cm ³)	6.871	6.866	6.863
temp (K)	293(2)	293(2)	293(2)
λ (Å)	0.71073	0.71073	0.71073
$F(000)$	1380	1380	1380
μ (mm ⁻¹)	51.853	51.818	51.799
θ (deg)	3.06–29.16	3.06–29.16	3.06–29.15
index range	$-12 \leq h \leq 12$	$-12 \leq h \leq 12$	$-12 \leq h \leq 12$
	$-12 \leq h \leq 12$	$-12 \leq h \leq 12$	$-12 \leq h \leq 12$
	$-13 \leq h \leq 13$	$-13 \leq h \leq 13$	$-13 \leq h \leq 13$
R_{int}	0.0817	0.0664	0.0728
reflections collected	7128	7152	7134
reflections ($I > 2\sigma(I)$)/independent reflections	555/590	533/591	536/592
data completeness	0.997	0.998	1.000
data/restraints/parameters	590/0/18	591/0/18	592/0/18
R/wR ($I > 2\sigma(I)$)	0.0376/0.0487	0.0315/0.0599	0.0394/0.0660
R/wR (all data)	0.0425/0.0494	0.0401/0.0620	0.0480/0.0684
GOF on F^2	1.419	1.211	1.176
largest diff peak and hole (e/Å ⁻³)	1.234 and -1.293	1.214 and -1.023	1.092 and -1.864

$$^a R(F) = \sum |F_o| - |F_c| / \sum |F_o|, wR(F_o^2) = [\sum w(F_o^2 - F_c^2)^2 / \sum w(F_o^2)^2]^{1/2}.$$

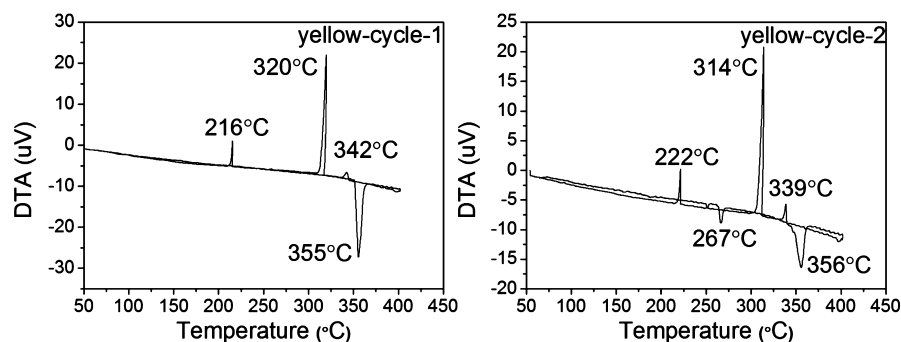


Figure 3. DTA curve of the yellow Tl_4CdI_6 sample. Heating and cooling rate $5^\circ\text{C}/\text{min}$.

Polarized light microscopy indicated that the yellow and red samples were single crystals. X-ray Laue back-reflection is another method to confirm the single-crystalline nature of the samples and allow determination of sample orientation. Yellow, red, and black samples show single crystalline by Laue X-ray back reflection. Figure S1 (Supporting Information) shows a Laue X-ray back-reflection pattern from a yellow Tl_4CdI_6 wafer, verifying its single crystalline nature.

The thermal behaviors of yellow, red, and black Tl_4CdI_6 crystal specimens were investigated with two consecutive cycles of heating and cooling using DTA measurements. All three types of crystals exhibited the same thermal behavior (Figure S2, Supporting Information). Hence, here we only present the behavior of the yellow specimens, which is shown in Figure 3. On heating the pure sample at $5^\circ\text{C}/\text{min}$, the DTA curve shows one endothermic peak at 355°C corresponding to a melting point. Upon cooling the melt, three sharp exothermic peaks are observed at 342 , 320 , and 216°C . Upon a second heating cycle of the same sample, there is one new endothermic peak at 267°C , in addition to the previously observed endothermic peak at 356°C . The slight shifting of the original DTA peaks and the appearance of new peaks indicate that the compound is incongruently melting. The powder XRD pattern of the sample obtained after two cycles of DTA shows the formation of TlCdI_3 ⁴⁸ and $\beta\text{-TlI}$ ^{49,50} (orthorhombic) in addition to Tl_4CdI_6 .

The exothermic peaks at 342 , 320 , and 216°C correspond to the crystallization of $\alpha\text{-TlI}$ ⁵¹ (cubic), Tl_4CdI_6 , and TlCdI_3 , respectively. The second endothermic peak at 267°C in cycle 2 corresponds to the melting of TlCdI_3 obtained from cycle 1. No peaks were observed during the DTA experiments that might be attributed to a phase transitions associated with TlI .^{52,53}

The phase relations during melting and crystallization observed in the DTA experiments were further confirmed by detailed in situ temperature-dependent synchrotron powder XRD analysis of a yellow sample. These experiments were carried out from room temperature to 356.5°C . Figure 4 shows the temperature dependence of synchrotron XRD patterns on heating and cooling at a rate of $20^\circ\text{C}/\text{h}$ with a 2θ range of 5° – 15° . The synchrotron XRD patterns at room temperature confirm the purity of the Tl_4CdI_6 phase. During the process of ramping the temperature up to 356.5°C , the cell volume of Tl_4CdI_6 increases smoothly as a function of temperature with no noticeable discontinuity. On cooling of the melt, $\alpha\text{-TlI}$ (cubic) crystallizes first and then Tl_4CdI_6 crystallizes below 329.6°C , indicating that Tl_4CdI_6 is an incongruently melting compound. No phase transition of Tl_4CdI_6 was observed on heating or cooling. The low-temperature phase $\beta\text{-TlI}$ crystallizes in the orthorhombic space group $Cmcm$ and

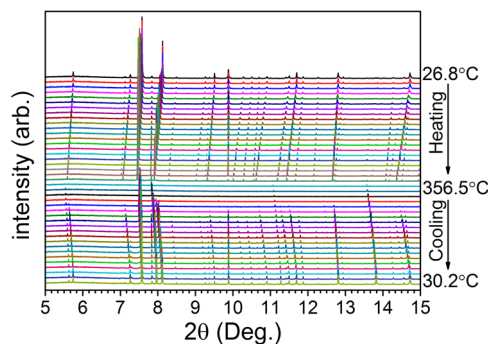


Figure 4. In situ temperature-dependent synchrotron XRD patterns of yellow Tl_4CdI_6 on heating and cooling.

transforms to the high-temperature cubic phase $\alpha\text{-TlI}$, which adopts the CsCl structure type at $\sim 170^\circ\text{C}$.^{52,53} The transformation is accompanied by a change in color of TlI from yellow to bright red. The phase transition of TlI is not observed in the synchrotron XRD patterns during the cooling process. As a result, tiny spots of red crystals ($\alpha\text{-TlI}$) were observed in the residues, followed by gradual color change to yellow ($\beta\text{-TlI}$) at room temperature.

Although Tl_4CdI_6 does not melt congruently, single crystals were still obtained by cooling of the stoichiometric melt using the vertical Bridgman method. Because the melting points of $\alpha\text{-TlI}$ and Tl_4CdI_6 are very close (about 20°C apart), the crystallizing range of $\alpha\text{-TlI}$ is narrow. That is why there is only one endothermic peak (355°C) upon heating on cycle 1. To reduce the crystallization time of $\alpha\text{-TlI}$, a faster pulling speed is suggested to pass over the crystallizing range. Nevertheless, because $\alpha\text{-TlI}$ crystallizes first, the liquid composition deviates from the proper stoichiometry. This leads to formation of TlI -poor low melting point phases after growth. This explains the impurities TlCdI_3 or $\text{Tl}_3\text{Cd}_2\text{I}_7$ ⁵⁴ at the top of the ingots, regardless of synthesis or crystal growth method. The added excess of TlI (5%) can suppress the formation of impurity phases, and it is easy to remove. After faster pulling during the growth, yellow single crystal could be obtained. Although Tl_4CdI_6 is the majority phase of the grown ingot, to obtain the highest quality crystal, only the middle part of the ingot should be selected for cutting and polishing.

The reason for different colors of the Tl_4CdI_6 is worth discussing. Dark gray, orange yellow, light yellow, green, red, and black crystals of Tl_4CdI_6 have been reported previously, but no explanation has been offered.^{40–43,45} From the temperature-dependent synchrotron powder XRD analysis, the color difference does not come from a phase transition. The small impurity of red $\alpha\text{-TlI}$ is considered to be the reason for the

different colors. The color of the pure phase of Tl_4CdI_6 is yellow. On cooling of the melt of Tl_4CdI_6 , red α -TII crystallizes first, and then it is encapsulated by subsequent Tl_4CdI_6 crystallization at the interface. The encapsulated small crystals of red α -TII in the Tl_4CdI_6 matrix are stabilized against the well-known phase transition.^{52,53} The longer the melt stays in the crystallization temperature range or alternatively if excess TII is present, the more α -TII will be obtained. Therefore, the apparent color of Tl_4CdI_6 single crystals can range from yellow to red and can even appear black if more α -TII is present. Interestingly, however the concentration of α -TII in the material is relatively low and cannot be detected by conventional powder XRD.

Thermal annealing is a commonly used processing method to improve the quality of semiconductor crystals, because it can reduce defects such as dislocations, vacancies, and antisite. Yellow, red, and black specimens of Tl_4CdI_6 were annealed under vacuum at 170 and 300 °C for 1 month, respectively. The colors did not change, which is consistent with the presence of α -TII second phase instead of defects in the crystal structure of Tl_4CdI_6 itself. Red and black (dark red) single crystals were shown to change to yellow after melting and quenching the melt from 400 °C in water. This quick cooling rate suppresses the formation of TII and gives a single phase of yellow Tl_4CdI_6 .

Single Crystal X-ray Diffraction. Tl_4CdI_6 crystallizes in the tetragonal crystal system with a centrosymmetric space group of $P4/mnc$, whether the crystal color is yellow, red, or black. All three types gave identical X-ray single crystal refinements. It is worthwhile to note that our cell parameters agree very closely with those found in the study by Beck and Milius.^{42,43} The structure is illustrated along the b -axis in Figure 5. The I atom is found in a five-coordination with a slightly

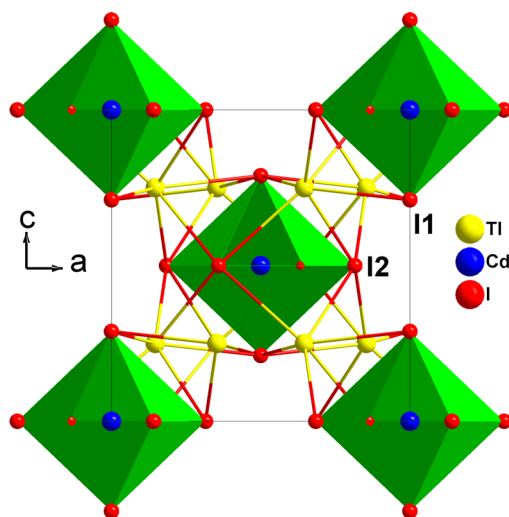


Figure 5. Crystal structure of Tl_4CdI_6 shown along the b -axis.

distorted square pyramid consisting of one Cd atom at the top and a square plane of four Tl atoms at the bottom. The Cd atom is coordinated to six I atoms to form a $[\text{CdI}_6]$ octahedron, while the Tl atom is coordinated by six I atoms in an extremely distorted trigonal antiprism. The adjacent $[\text{CdI}_6]$ octahedra are connected to each other by sharing the faces with $[\text{TlI}_6]$ antiprisms, resulting in the final tetragonal crystal structure. Because of the strong covalent bonding of Cd–I and weak bonding of Tl–I, the crystal structure suggests a probability of

defects and impurities in single crystals. The 3D structure of Tl_4CdI_6 is likely to result in larger band gap and enhanced mechanical properties compared to layered semiconductor materials, making it suitable for further processing and applications.

Spectroscopy. To accurately investigate the optical properties of Tl_4CdI_6 and check for possible defect or impurity states, we measured the reflectance, transmittance, Raman, and photoluminescence spectra of single crystals. UV–vis diffuse reflectance spectra were collected for yellow, red, and black crystalline powders of Tl_4CdI_6 at room temperature, as shown in Figure 6a.^{55a,b} They all show a sharp band gap of 2.83 eV, except that there is one broad weak absorption peak at 2.28 eV in both the red and black samples. To confirm the band gap of Tl_4CdI_6 and probe its direct or indirect nature, transmittance (T) and reflectance (R) spectra were recorded from single crystals.

From T and R, the absorption coefficient (α) can be determined as a function of incident photon energy.^{55c} For indirect band gaps, a linear fit to $\alpha^{1/2}$ versus energy gives the indirect band gap as an intercept with the x -axis, whereas direct band gaps show a linear fit to α^2 . As shown in Figure 6b, a linear fit to α^2 versus energy gives a direct gap 2.81 eV for both yellow and red single crystals. Moreover, one broad and weak absorption peak at 2.28 eV can be observed in the red samples on the α^2 vs E curves but not in the yellow samples. The pure phase of Tl_4CdI_6 is yellow in transmitted light, in agreement with the band gap. Likewise, the colors of red and black correspond to the absorption of the low photon energy at 2.28 eV, which comes from the encapsulated α -TII⁵⁶ impurity discussed above. The band gap of β -TII^{57,58} is 2.75 eV. Clearly, the optical absorption spectra of Tl_4CdI_6 suggest that it is well-suited for X-ray and γ -ray detection at room temperature, because the band gap is large enough to avoid thermally generated carriers.

The Raman spectrum (Figure S3, Supporting Information) obtained for Tl_4CdI_6 shows a single peak centered at 117 cm^{-1} , regardless of color. This peak is assigned to symmetric vibrations of the nearly perfect $[\text{CdI}_6]$ octahedron.^{40,41} The TII second phase impurity is too low in concentration to be detected by Raman spectroscopy.

Analysis of the photoluminescent behavior of Tl_4CdI_6 is useful in providing information about impurities and structural defects. PL was observed at low temperatures for the yellow crystals of Tl_4CdI_6 (Figure 7a). At -243.15 °C, intense emission is seen at 2.4 eV. As the temperature is increased to -233.15 °C, the peak intensity decreases to allow two other peaks to be discerned. Further analysis reveals that these can be decomposed by a Gaussian function to reveal peaks with energies of 2.82 and 3.0 eV, as shown in Figure 7b. The presence of the peak at 2.4 eV is considered to be a result of the α -TII impurity. This peak should correspond to the absorption peak at 2.28 eV in the UV–vis spectrum at room temperature, which often blue shifts at low temperatures.⁵⁹ The band gap of Tl_4CdI_6 is ~ 2.8 eV at room temperature and is expected to shift to ~ 2.9 or 3.0 eV at low temperature. The peak at 3.0 eV correspond to this shift. Detailed analyses, peak assignments, correlations with donor and acceptor levels, and assessment of the temperature dependence of the PL peaks are ongoing and will be reported elsewhere.

Electronic Structure. To understand the nature of the band gap and band edges of Tl_4CdI_6 , we calculated the projected density of states (PDOS) and the projected band

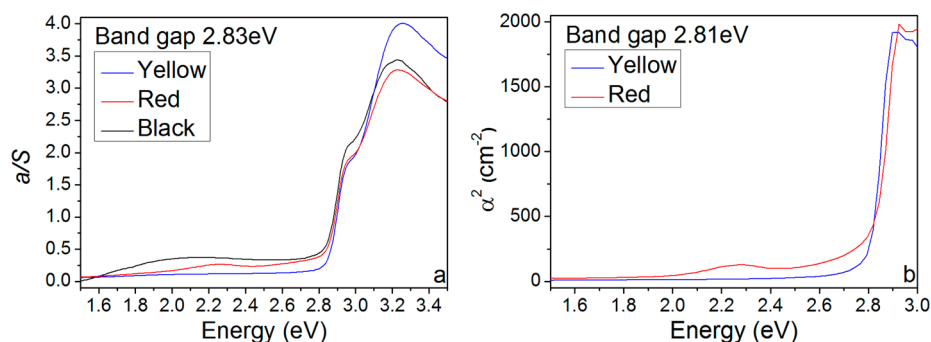


Figure 6. Optical band gap of Tl_4CdI_6 . (a) Single crystal transmission spectrum. (b) Diffuse reflectance spectrum of a polycrystalline sample.

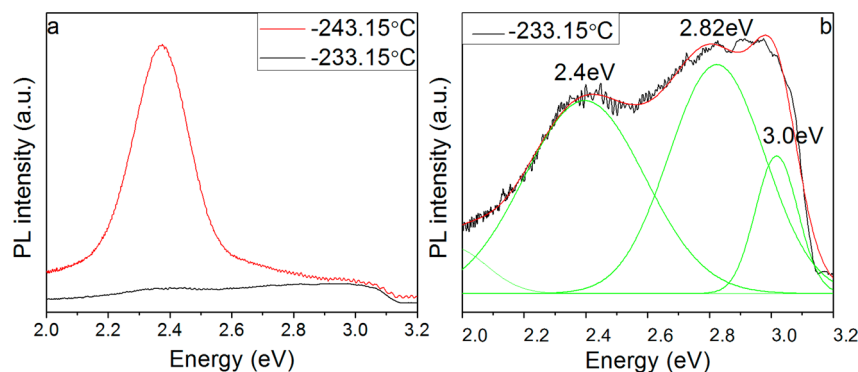


Figure 7. Photoluminescence spectra of yellow Tl_4CdI_6 . (a) At -243.15°C , one peak is seen at 2.37 eV, which corresponds to the green fluorescence. The emission intensity at -233.15°C is significantly decreased, and a broad emission spectrum is seen. (b) At -233.15°C , three peaks can be resolved using a Gaussian model with energies of 2.4, 2.82, and 3.0 eV.

structure using the LDA functional. When SOC is not included, the valence band maximum (VBM) consists of I-p and Tl-s orbitals. As shown in Figure 8a, the major contribution to the valence bands is I-p orbitals, but near the top of the valence band, the hybridization with Tl-s orbital becomes significant. Due to the extended and isotropic character of the Tl-s state, the VBM is highly dispersive and isotropic (Figure 8c). On the other hand, the conduction band minimum (CBM) is composed of Cd-s, Tl-p, and I-p orbitals. Compared to the VBM, the CBM is less isotropic and less dispersive. This is consistent with the fact that the 5s state (Cd) is less extended than the 6s state (Tl). However, when we turn on SOC, the CBM is severely changed while the VBM is unchanged; the Tl-p state at the CBM is more shifted down than the Cd-s state because of the larger SOC strength of Tl. Then, as shown in Figure 8b,d, Tl-p orbitals become a major component of the CBM, which leads to more isotropic and parabolic band dispersion. This result indicates that Tl_4CdI_6 has isotropic and parabolic band edges at both VBM and CBM, which give light effective masses of hole and electron.

In order to obtain a more accurate band gap, which is usually underestimated in the LDA calculation, we further carried out the sX-LDA band structure calculation with SOC (Figure 8e). Compared to the LDA with SOC band structure in Figure 8d, the overall feature is mostly maintained, but the band gap is increased. The band gap of Tl_4CdI_6 is predicted to be direct at Γ and 2.25 eV, which is still considerably smaller than the experimental one. On the basis of the sX-LDA band structure calculation, we also estimated hole and electron effective masses at the respective band edges; the hole effective mass at the VBM is $0.44 m_e$ and the electron effective mass at the CBM is $0.30 m_e$, along the Γ to Z direction. Thus, in terms of band gap

and effective mass, Tl_4CdI_6 can be a good platform for the γ -ray detector.

Electrical and Photoelectrical Characterization. Dark current suppression is of primary importance in detector fabrication because it is detrimental to energy resolution due to leakage noise. To prevent this, it is important to maximize the resistivity of the material. High resistivities permit higher bias voltages and hence longer drift lengths of the generated carriers. A minimum resistivity of $\sim 10^8$ – $10^9 \Omega\cdot\text{cm}$ is generally recommended for room temperature operation, and detector-grade CZT has resistivities of $\sim 10^{11} \Omega\cdot\text{cm}$. The current–voltage characteristics of yellow (Figure 9a), red, and black (Figure S4, Supporting Information) single crystals were measured parallel to the c -axis. The shape of the I – V curve is linear, indicating that the contacts were ohmic instead of forming a Schottky barrier, which is a common phenomenon with detector-grade materials. The measured electrical resistivities are 6.10×10^{10} , 5.39×10^{10} , and $1.18 \times 10^{10} \Omega\cdot\text{cm}$ for the yellow, red, and black crystals, respectively. These values are comparable to that of CZT. This indicates that the impurities and defects do not have a notable influence on resistivity.

The $\mu\tau$ product of the electron and hole carriers determines the charge collection efficiency and is the key figure of merit to evaluate the performance of semiconductor materials for their radiation detection efficiency. The generated carriers must reach the electrodes in order to be measured. The drift length (λ) in the device is given by $\lambda = \mu\tau E$, where E is the electric field in the material. Hence, high $\mu\tau$ products result in better response to radiation and to high-resolution detection. In order to determine the $\mu\tau$ product for both electrons and holes, the photoconductivity measurements were performed on suitably

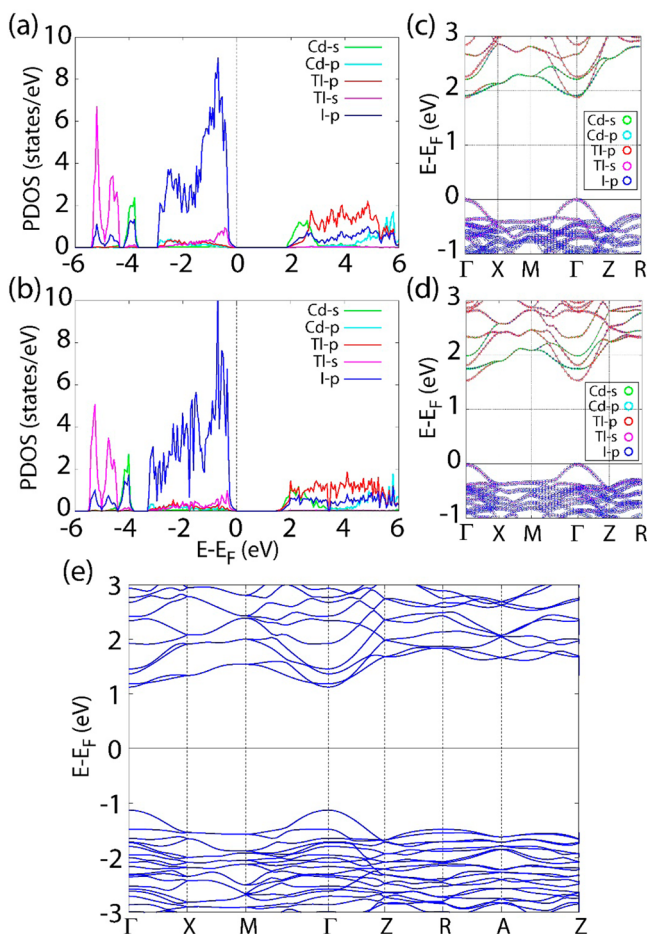


Figure 8. Orbital projected density of states: (a) LDA without SOC and (b) LDA with SOC. Orbital projected band structures: (c) LDA without SOC and (d) LDA with SOC. Each orbital is denoted by green for Cd-s, light blue for Cd-p, red for Tl-p, pink for Tl-s, and blue for I-p. The sX-LDA band structure with SOC is presented in part e.

sized Tl_4CdI_6 crystals using visible-light irradiation. The photon energy of the laser beam was higher than the band gap energy of the material, and therefore, we can determine the $\mu\tau$ product for intrinsic excitation case. Different voltage polarities are applied to the illuminated electrode so that the photocurrent for both carrier types are measured separately and their corresponding $\mu\tau$ products obtained. For strongly absorbed

light, the photoconductivity can be modeled using the following so-called Many equation:⁶⁰

$$I(U) = \frac{I_0 \mu \tau U}{L^2} \left(1 - \exp\left(\frac{-L^2}{\mu \tau U}\right) \right) \quad (1)$$

Here, I is the photocurrent, I_0 is the saturation current, L is the sample thickness, U is the applied voltage, and s is the surface recombination velocity.

In CZT, the $\mu\tau$ values obtained from our photoconductivity measurements are in good agreement with measurements using ionizing radiation, which confirms the reliability of our $\mu\tau$ values. From the analysis of photocurrent response with respect to applied bias voltage, $\mu\tau$ products and the carrier surface recombination parameter s/μ were calculated. The value of s/μ can be used as an evaluation criterion for surface quality. Photoconductivity measurements with wavelengths above the band gap are particularly sensitive to surface recombination, because photon absorption occurs in the vicinity of the surface. A lower quality surface is expected to increase recombination effects and thus reduce the charge collection efficiency. Consequently, the s/μ should be minimized to optimize detector performance. Surface recombination is particularly strong for cut and polished wafers and less pronounced for cleaved surfaces. With better polishing method, the s/μ value can be reduced considerably.

Parts b and c of Figure 9 show the electron and hole photoconductivity curves for the yellow Tl_4CdI_6 single crystal. Fitting of the data to formula 1, the $\mu\tau$ values were obtained for electrons and holes of all samples and are summarized in Table 2. The $\mu\tau$ products for the yellow Tl_4CdI_6 sample are calculated to be $(\mu\tau)_e = 6.05 \times 10^{-4} \text{ cm}^2/\text{V}$ for electrons and $(\mu\tau)_h = 1.00 \times 10^{-4} \text{ cm}^2/\text{V}$ for holes. The $\mu\tau$ values are moderately high albeit lower than those of high-performance commercial grade CZT [$(\mu\tau)_e = 4.5 \times 10^{-2} \text{ cm}^2/\text{V}$, $(\mu\tau)_h = 1.0 \times 10^{-4} \text{ cm}^2/\text{V}$] and higher than those for other detector-grade crystals, such as HgI_2 [$(\mu\tau)_e = 8 \times 10^{-4} \text{ cm}^2/\text{V}$, $(\mu\tau)_h = 3 \times 10^{-5} \text{ cm}^2/\text{V}$].⁶¹ The mobility-lifetime product $\mu\tau$ values for the red and black Tl_4CdI_6 samples (Figure S5, Supporting Information) show the same order of magnitude compared to the yellow samples, which suggest that the impurities and defects do not have a notable influence on charge transport. These results are very promising, because these high $\mu\tau$ values were obtained without any further purification made on the purchased starting materials. Future experiments involving extensive purification

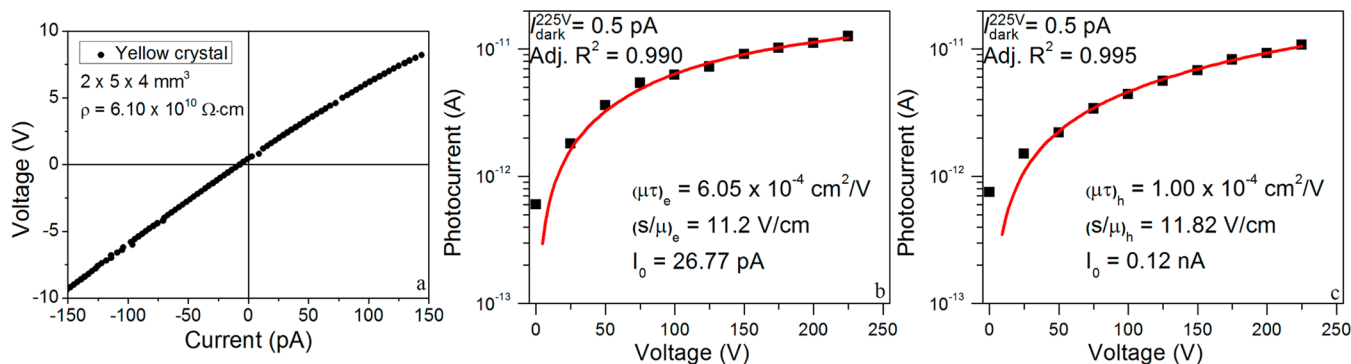
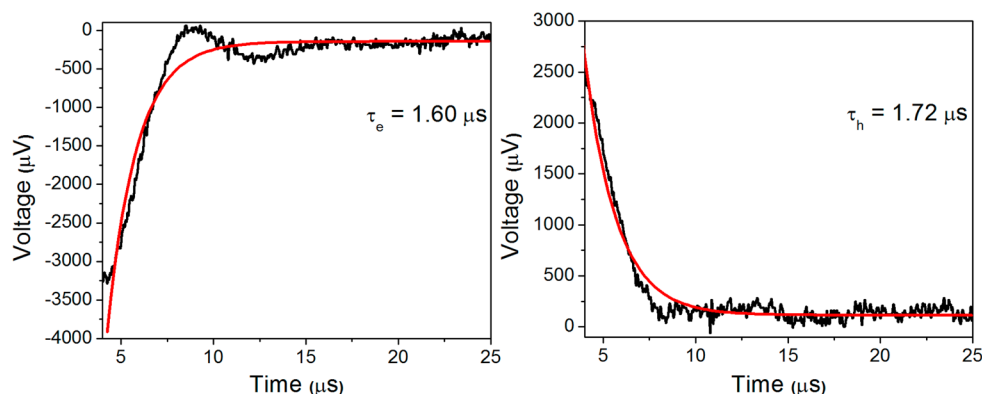


Figure 9. Resistivity and photoconductivity of yellow Tl_4CdI_6 sample. (a) Current–voltage characteristics. Photocurrent versus applied voltage (b) for electrons and (c) for holes.

Table 2. Summary of the Physical Properties of Ti_4CdI_6

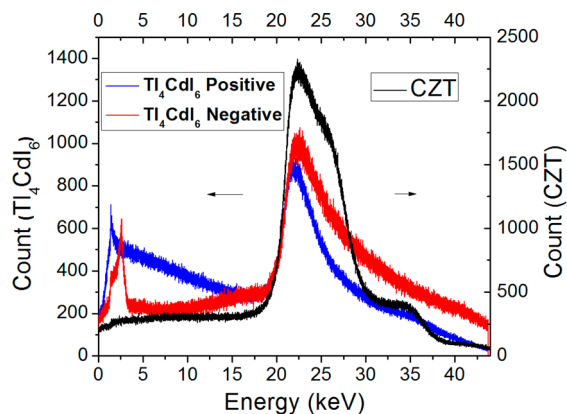
Ti_4CdI_6	density (g/cm^3)	band gap (eV)	resistivity ($\Omega\text{-cm}$)	$(\mu\tau)_e$ (cm^2/V)	$(\mu\tau)_h$ (cm^2/V)	τ_e (s)	τ_h (s)
yellow	6.871	2.83	6.10×10^{10}	6.05×10^{-4}	1.00×10^{-4}	1.60	1.72
red	6.866	2.83	5.39×10^{10}	1.18×10^{-4}	1.95×10^{-5}		
black	6.863	2.83	1.18×10^{10}	4.03×10^{-4}	2.65×10^{-4}		

Figure 10. Photocurrent versus time of (a) electron and (b) hole carriers, measured on a yellow Ti_4CdI_6 sample.

of these materials as well as improving crystal growth procedures that we described here are likely to further increase the resistivity of Ti_4CdI_6 and enhance $\mu\tau$ values (by reducing scattering centers such as impurities and native defects).

For minority carrier lifetime measurements, the sample was exposed to a nitrogen-pulsed laser excitation. Photoexcited carrier concentration rose exponentially with time when the sample was exposed to the laser. Since the excitation pulse width (t_{NL}), is short compared to τ , the minority carrier lifetime ($t_{\text{NL}} \ll \tau$), the photogenerated carrier concentration does not reach a steady-state value. Under this condition the decay of the minority carrier concentration $\Delta p_{\text{mi}}(t)$ upon cessation of the optical pulse is given by $\Delta p_{\text{mi}}(t) = t_{\text{NL}} G_{\text{ph}} \exp(-t/\tau)$,⁶² where G_{ph} is photogeneration rate. Here $t = 0$ corresponds to the moment when the laser pulse ends. The decay of photocurrent is given by $i_{\text{p1}} = i_{\text{p0}} \exp(-t/\tau)$,⁵⁵ where i_{p0} is the photoinduced current at $t = 0$. By measuring the transient current responses of electron and hole carriers, we are able to determine what the minority carrier is and evaluate its lifetime. Figure 10 shows the photocurrent versus time for electrons and holes for the yellow Ti_4CdI_6 single crystal measured at 25 °C. The black curves are the measured data sets, whereas the red curves are calculated values using the equation above. The electron recombination time of Ti_4CdI_6 was estimated to be 1.60 μs and for the hole carriers 1.72 μs . In this case, the minority carrier is the electron. From the previously reported $\mu\tau$ measurements and recombination lifetime measurements reported here, the drift mobility of the compounds can be estimated. The estimated mobility value of minority carriers (electron) is 378 $\text{cm}^2/\text{V}\cdot\text{s}$ for Ti_4CdI_6 . Both μ_e and τ_e values are very much comparable with up-to-date measurements on CZT.⁶³ Details regarding material properties such as density, optical absorption, current–voltage (I – V) relations, and photoconductivity are given in Table 2.

Detector Properties. To investigate whether hard X-rays are detectable by the Ti_4CdI_6 wafers, we performed preliminary white Ag X-ray irradiation experiments at room temperature. The pulse height spectrum obtained for a detector using a $5 \times 7 \times 1.6$ mm yellow Ti_4CdI_6 crystal is shown in Figure 11 with the corresponding X-ray spectrum from a commercial CZT detector, using a $5 \times 5 \times 2$ mm CZT wafer shown for

Figure 11. Spectral responses of Ti_4CdI_6 sample with positive bias (blue curve) and negative bias (red curve) as compared to that of a commercial CZT detector sample under a Ag X-ray source.

comparison. The characteristic lines of Ag $K\alpha$ of 22.4 keV were resolved for both positive and negative biases applied to the Ti_4CdI_6 sample. To estimate the counting efficiency, we divided the counting over the areas of our Ti_4CdI_6 and CZT detectors, respectively. From the normalized counting, the sensitivity of the response corresponds to approximately 32% of the commercial CZT detector. This is a very promising result, as there is a great potential for improvement of radiation detection resolution and signal strength with optimization of Ti_4CdI_6 crystal growth parameters in the future.

CONCLUSIONS

The correct color of Ti_4CdI_6 is yellow. The present study has demonstrated that Ti_4CdI_6 is a promising candidate material for X- and γ -ray radiation detection. The Ti_4CdI_6 compound was synthesized using TII and CdI_2 as starting materials by a direct-combination, solid-state melting reaction. Despite its incongruent melting, if growth is carried out with a slight excess of TII and by applying a relatively fast translation speed, large single crystals of yellow Ti_4CdI_6 can be grown with the Bridgman method. This compound is a direct band gap semiconductor that combines a set of useful physical properties

for successful detection that is challenging to achieve in a single material, such as high atomic number, high density, wide band gap, high electrical resistivity, and significant photoconductivity response. Low concentrations of α -TlI impurity are responsible for leading to different colors of single crystals of Ti_4CdI_6 during the synthesis or crystal growth, but interestingly, they do not appear to significantly affect crystal quality or charge transport properties. The potential of Ti_4CdI_6 as a crystal for detection of hard radiation is indeed highlighted by the ability of our unoptimized crystalline wafers to detect and resolve Ag X-ray radiation. Further improvements in crystal growth, wafer fabrication, and device processing of Ti_4CdI_6 should result in large increases in detector performance for room temperature operation.

■ ASSOCIATED CONTENT

Supporting Information

An experimental section, including single crystal X-ray diffraction, powder X-ray diffraction, elemental analysis, differential thermal analysis, UV–vis diffuse reflectance and single crystal spectroscopy, Raman spectroscopy, photoluminescence, electrical resistivity, photoconductivity measurements, and band structure calculations; Tables S1–S3, summarizing atomic positions and isotropic displacement factors for Ti_4CdI_6 ; Figure S1, the X-ray Laue back-reflection photographs of Ti_4CdI_6 single crystal; Figure S2, DTA curve of the red and black Ti_4CdI_6 crystals; Figure S3, Raman spectrum of Ti_4CdI_6 ; Figure S4, current versus voltage characteristics of red and black Ti_4CdI_6 single crystals; and Figure S5, photocurrent versus applied voltage for electrons and holes on red and black Ti_4CdI_6 crystals. This material is available free of charge via the Internet at <http://pubs.acs.org>.

■ AUTHOR INFORMATION

Corresponding Author

*E-mail: m-kanatzidis@northwestern.edu.

Notes

The authors declare no competing financial interest.

■ ACKNOWLEDGMENTS

This work is supported in part by the Department of Homeland Security with grant No. 2010-DN-077-ARI042-02. Use of the Advanced Photon Source at Argonne National Laboratory was supported by the U.S. Department of Energy, Office of Science, and Office of Basic Energy Sciences.

■ REFERENCES

- (1) McGregor, D. S.; Hermon, H. *Nucl. Instrum. Methods Phys. Res., Sect. A* **1997**, 395, 101.
- (2) Sellin, P. J. *Nucl. Instrum. Methods Phys. Res., Sect. A* **2003**, 513, 332.
- (3) Owens, A.; Peacock, A. *Nucl. Instrum. Methods Phys. Res., Sect. A* **2004**, 531, 18.
- (4) Devanathan, R.; Corrales, L. R.; Gao, F.; Weber, W. J. *Nucl. Instrum. Methods Phys. Res., Sect. A* **2006**, 565, 637.
- (5) Owens, A. *J. Synchrotron Radiat.* **2006**, 13, 143.
- (6) Milbrath, B. D.; Peurrung, A. J.; Bliss, M.; Weber, W. J. *J. Mater. Res.* **2008**, 23, 2561.
- (7) Lachish, U. *J. Cryst. Growth* **2001**, 225, 114.
- (8) Szeles, C. *Phys. Status Solidi B* **2004**, 241, 783.
- (9) Schlesinger, T. E.; Toney, J. E.; Yoon, H.; Lee, E. Y.; Brunett, B. A.; Franks, L.; James, R. B. *Mater. Sci. Eng., R* **2001**, 32, 103.
- (10) Burger, A.; Groza, M.; Cui, Y.; Hillman, D.; Brewer, E.; Bilikiss, A.; Wright, G. W.; Li, L.; Fu, F.; James, R. B. *J. Electron. Mater.* **2003**, 32, 756.
- (11) Ponpon, J. P. *Nucl. Instrum. Methods Phys. Res., Sect. A* **2005**, 551, 15.
- (12) Sellin, P. J. *Nucl. Instrum. Methods Phys. Res., Sect. A* **2006**, 563, 1.
- (13) Owens, A.; Bavdaz, M.; Lisjutin, I.; Peacock, A.; Sipila, H.; Zatoloka, S. *Nucl. Instrum. Methods Phys. Res., Sect. A* **2001**, 458, 413.
- (14) Hitomi, K.; Tada, T.; Kim, S. Y.; Wu, Y.; Tanaka, T.; Shoji, T.; Yamazaki, H.; Ishii, K. *IEEE Trans. Nucl. Sci.* **2011**, 58, 1987.
- (15) Kim, H.; Kargar, A.; Cirignano, L.; Churilov, A.; Ciampi, G.; Higgins, W.; Olschner, F.; Shah, K. *IEEE Trans. Nucl. Sci.* **2012**, 59, 243.
- (16) Shah, K. S.; Bennett, P.; Klugerman, M.; Moy, L.; Cirignano, L.; Dmitriyev, Y.; Squillante, M. R.; Olschner, F.; Moses, W. W. *IEEE Trans. Nucl. Sci.* **1997**, 44, 448.
- (17) Deich, V.; Roth, M. *Nucl. Instrum. Methods Phys. Res., Sect. A* **1996**, 380, 169.
- (18) Owens, A.; Bavdaz, M.; Brammertz, G.; Krumrey, M.; Martin, D.; Peacock, A.; Troger, L. *Nucl. Instrum. Methods Phys. Res., Sect. A* **2002**, 479, 535.
- (19) van den Berg, L.; Vigil, R. D. *Nucl. Instrum. Methods Phys. Res., Sect. A* **2001**, 458, 148.
- (20) Amman, M.; Lee, J. S.; Luke, P. N. *J. Appl. Phys.* **2002**, 92, 3198.
- (21) Bolotnikov, A. E.; Camarda, G. S.; Carini, G. A.; Cui, Y.; Li, L.; James, R. B. *Nucl. Instrum. Methods Phys. Res., Sect. A* **2007**, 571, 687.
- (22) Komar, V.; Gektin, A.; Nalivaiko, D.; Klimenko, I.; Migal, V.; Panchuk, O.; Rybka, A. *Nucl. Instrum. Methods Phys. Res., Sect. A* **2001**, 458, 113.
- (23) Chen, H.; Awadalla, S. A.; Mackenzie, J.; Redden, R.; Bindley, G.; Bolotnikov, A. E.; Camarda, G. S.; Carini, G. *IEEE Trans. Nucl. Sci.* **2007**, 54, 811.
- (24) Bolotnikov, A. E.; Camarda, G. C.; Wright, G. W.; James, R. B. *IEEE Trans. Nucl. Sci.* **2005**, 52, 589.
- (25) Gasperino, D.; Bliss, M.; Jones, K.; Lynn, K.; Derby, J. J. *J. Cryst. Growth* **2009**, 311, 2327.
- (26) Triboulet, R. In *Phys. Status Solidi C*; Stutzmann, M., Ed. 2005; Vol. 2, p 1556.
- (27) Kim, H.; Cirignano, L.; Churilov, A.; Ciampi, G.; Higgins, W.; Olschner, F.; Shah, K. *IEEE Trans. Nucl. Sci.* **2009**, 56, 819.
- (28) Georgeson, G.; Milstein, F. *Nucl. Instrum. Methods Phys. Res., Sect. A* **1989**, 285, 507.
- (29) Hayashi, T.; Kinpara, M.; Wang, J. F.; Mimura, K.; Isshiki, M. *J. Cryst. Growth* **2008**, 310, 47.
- (30) He, Y.; Zhu, S. F.; Zhao, B. J.; Jin, Y. R.; He, Z. Y.; Chen, B. J. *J. Cryst. Growth* **2007**, 300, 448.
- (31) Li, W. T.; Li, Z. H.; Zhu, S. F.; Yin, S. J.; Zhao, B. J.; Chen, G. X. *Nucl. Instrum. Methods Phys. Res., Sect. A* **1996**, 370, 435.
- (32) Androulakis, J.; Peter, S. C.; Li, H.; Malliakas, C. D.; Peters, J. A.; Liu, Z. F.; Wessels, B. W.; Song, J. H.; Jin, H.; Freeman, A. J.; Kanatzidis, M. G. *Adv. Mater.* **2011**, 23, 4163.
- (33) Johnsen, S.; Liu, Z. F.; Peters, J. A.; Song, J. H.; Nguyen, S.; Malliakas, C. D.; Jin, H.; Freeman, A. J.; Wessels, B. W.; Kanatzidis, M. G. *J. Am. Chem. Soc.* **2011**, 133, 10030.
- (34) Johnsen, S.; Liu, Z. F.; Peters, J. A.; Song, J. H.; Peter, S. C.; Malliakas, C. D.; Cho, N. K.; Jin, H. S.; Freeman, A. J.; Wessels, B. W.; Kanatzidis, M. G. *Chem. Mater.* **2011**, 23, 3120.
- (35) Liu, Z. F.; Peters, J. A.; Wessels, B. W.; Johnsen, S.; Kanatzidis, M. G. *Nucl. Instrum. Methods Phys. Res., Sect. A* **2011**, 659, 333.
- (36) Li, H.; Peters, J. A.; Liu, Z. F.; Sebastian, M.; Malliakas, C. D.; Androulakis, J.; Zhao, L. D.; Chung, I.; Nguyen, S. L.; Johnsen, S.; Wessels, B. W.; Kanatzidis, M. G. *Cryst. Growth Des.* **2012**, 12, 3250.
- (37) Johnsen, S.; Peter, S. C.; Nguyen, S. L.; Song, J. H.; Jin, H.; Freeman, A. J.; Kanatzidis, M. G. *Chem. Mater.* **2011**, 23, 4375.
- (38) Ilyasov, I. I.; Bergman, A. G. *Russ. J. Inorg. Chem.* **1959**, 4, 414.
- (39) Ilyasov, I. I.; Dionisev, S. D.; Bergman, A. G. *Russ. J. Inorg. Chem.* **1962**, 7, 318.

- (40) Ammlung, R. L.; Shriver, D. F.; Kamimoto, M.; Whitmore, D. H. *J. Solid State Chem.* **1977**, *21*, 185.
- (41) Orinchai, A. V.; Lazarev, V. B.; Peresh, E. Y.; Koperlos, B. M.; Dordyai, V. S. *Inorg. Mater.* **1982**, *18*, 1080.
- (42) Beck, H. P.; Milius, W. Z. *Anorg. Allg. Chem.* **1986**, 539, 7.
- (43) Beck, H. P.; Milius, W. Z. *Anorg. Allg. Chem.* **1988**, 562, 105.
- (44) Nair, S. M.; Rafiuddin, Y. A. I.; Ahmad, A. *Solid State Ionics* **1996**, 86–8, 137.
- (45) Franiv, A. V.; Kushnir, O. S.; Girnyk, I. S.; Franiv, V. A.; Kityk, I.; Piasecki, M.; Plucinski, K. J. *Ukr. J. Phys. Opt.* **2013**, *14*, 6.
- (46) Seltzer, S. M. *Radiat. Res.* **1993**, 136, 147.
- (47) Laugier, J.; Filhol, A. J. *Appl. Crystallogr.* **1983**, *16*, 281.
- (48) Zandbergen, H. W.; Verschoor, G. C.; Ijdo, D. J. W. *Acta Crystallogr. Sect. B-Struct. Sci.* **1979**, *35*, 1425.
- (49) Helmholtz, L. Z. *Kristallogr.* **1936**, *95*, 129.
- (50) Becker, D.; Beck, H. P. Z. *Kristallogr.* **2004**, *219*, 348.
- (51) Blackman, M.; Khan, I. H. *Proc. Phys. Soc. London* **1961**, *77*, 471.
- (52) Samara, G. A.; Walters, L. C.; Northrop, D. A. *J. Phys. Chem. Solids* **1967**, *28*, 1875.
- (53) Vandyke, J. P.; Samara, G. A. *Phys. Rev. B* **1975**, *11*, 4935.
- (54) Petrov, V. V.; Bogdanova, A. V.; Mashkarinets, E. K.; Belskii, V. K.; Gladyshevskii, E. I.; Mokraya, I. R.; Pecharskii, V. K. *Inorg. Mater.* **1987**, *23*, 1238.
- (55) (a) Armatas, G. S.; Kanatzidis, M. G. *Science* **2006**, *313*, 817–820. (b) Armatas, G. S.; Kanatzidis, M. G. *Nature* **2006**, *441*, 1122–1125. (c) Smith R. A. *Semiconductors*. Cambridge University Press: Cambridge, UK, 1959.
- (56) Dovgii, Y. O.; Kityk, I. V.; Kolinko, M. I.; Krochuk, A. S.; Franiv, A. V.; Zamorskii, M. K. *Phys. Status Solidi B* **1991**, *167*, 637.
- (57) Ohno, N.; Itoh, M. *J. Phys. Soc. Jpn.* **1993**, *62*, 2966.
- (58) Kolinko, M. I.; Kityk, I. V.; Krochuk, A. S. *J. Phys. Chem. Solids* **1992**, *53*, 1315.
- (59) Kutsyk, M. V.; Pidzyrilo, M. S. *J. Lumin.* **1998**, *79*, 135.
- (60) Many, A. J. *Phys. Chem. Solids* **1965**, *26*, 575.
- (61) Kargar, A.; Ariesanti, E.; McGregor, D. S. *Nucl. Technol.* **2011**, *175*, 131.
- (62) Kasap, S. O. *Principles of Electronic Materials and Devices*; McGraw-Hill: Boston, MA, 2002.
- (63) Cho, H. Y.; Lee, J. H.; Kwon, Y. K.; Moon, J. Y.; Lee, C. S. *J. Instrum.* **2011**, *6*, C01025.